Smart Structures and Systems, *Vol. 21, No. 3 (2018) 373-387*
DOI: https://doi.org/10.12989/sss.2018.21.3.373

Semi-active leverage-type isolation system considering minimum structural energy

Tzu-Kang Lin[*1], Lyan-Ywan Lu[2a] and Chi-Jen Chen[1b]

[1]*Department of Civil Engineering, National Chiao Tung University, 1001 University Road, Hsinchu 300, Taiwan*
[2]*Department of Civil Engineering, National Cheng Kung University, 1 University Road, Tainan 701, Taiwan*

(Received October 12, 2017, Revised February 14, 2018, Accepted February 16, 2018)

Abstract. Semi-active isolation systems based on leverage-type stiffness control strategies have been widely studied. The main concept behind this type of system is to adjust the stiffness in the isolator to match the fundamental period of the isolated system by using a simple leverage mechanism. Although this system achieves high performance under far-field earthquakes, it is unsuitable for near-fault strong ground motion. To overcome this problem, this study considers the potential energy effect in the control law of the semi-active isolation system. The minimal energy weighting (MEW) between the potential energy and kinetic energy was first optimized through a series of numerical simulations. Two MEW algorithms, namely generic and near-fault MEW control, were then developed to efficiently reduce the structural displacement responses. To demonstrate the performance of the proposed method, a two-degree-of-freedom structure was employed as a benchmark. Numerical results indicate that the dynamic response of the structure can be effectively dampened by the proposed MEW control under both far-field and near-fault earthquakes, whereas the structural responses resulting from conventional control methods may be greater than those for the purely passive control method. Moreover, according to experimental verifications, both the generic and near-fault MEW control modes yielded promising results under impulse-like earthquakes. The practicability of the proposed control algorithm was verified.

Keywords: semi-active control; near-fault earthquake; potential energy

1. Introduction

Large-scale earthquake events often result in considerable casualties and can also cause structures in the affected area to collapse. To prevent loss of life and property due to earthquakes, researchers have focused on dampening the structural responses.

Structure control systems have been under development for several decades. Such systems can be mainly classified into three categories: passive, active, and semi-active control. Passive control systems have advantages such as low control energy and reliability and effectiveness of control. For instance, a triangular-plate added damping and stiffness device (TADAS) was developed by Tsai *et al.* (1993). Hybrid damper actuator bracing control was proposed by Zhang *et al.* (2006), in which bracing equipment is installed on the floor and linked to energy-absorbing dampers. Several studies (Tamura *et al.* 1995, Martinez Rueda 2002, De la Cruz *et al.* 2007) have revealed that structural reactions can be ameliorated by utilizing dampers on the structure.

*Corresponding author, Associate Professor
E-mail: tklin@nctu.edu.tw
[a] Professor
E-mail: lylu@mail.ncku.edu.tw
[b] Master Student
E-mail: mortimermoon@hotmail.com

An active control device used in combination with a control algorithm often produces results superior to those of a passive control system. The first phase of a comprehensive experimental study concerning the possible application of active control to structures under seismic excitations was presented by Chung *et al.* (1998). A dynamic fluid control device was proposed by Battista *et al.* (2008); use of the device involves placing multiple parallel tubes on the top of the structure and connecting a rotating device below to adjust the device direction. The response of the structure can be attenuated by arranging the tubes along the excitation direction.

Although passive control is reliable, in most cases, its control effectiveness cannot compare to that of active control systems. Despite better performance, control robustness is a problem for active control systems. To combine the merits of both active and passive control systems, semi-active control has been developed. Yang *et al.* (2000) installed a resettable damper in the isolation layer for seismic response control. A hybrid-control-based isolation system that included a magnetorheological (MR) damper and fuzzy control was proposed by Lin *et al.* (2007). A semi-active isolation system called a resettable variable stiffness damper (RVSD) was proposed by Lu *et al.* (2009); the effectiveness of the system in displacement control was demonstrated. An application of an active tuned mass damper (ATMD) for controlling the seismic response of an 11-story building was demonstrated by Shariatmadar and Razavi (2014). The global controller was achieved by combining a fuzzy logic controller (FLC) and the particle

ISSN: 1738-1584 (Print), 1738-1991 (Online)

swarm optimization (PSO) method. The results showed that the proposed system decreases the peak displacement of the top floor by about 10%-30% more than that of the FLC system.

For adaptive stiffness control, the potential of using a semi-active controllable stiffness device whose spring coefficient can be modulated in real-time for tonal disturbance rejection applications was examined by Anusonti-Inthra (2003). A short time Fourier transformation (STFT) control algorithm based on a semiactive independently variable stiness (SAIVS) device was proposed and numerically evaluated by Narasimhana and Nagarajaiah (2005). A new moving average non-linear tangential stiffness control algorithm for control of the SAIVS device was further developed and experimentally verified by Nagarajaiah and Sahasrabudhe (2006). A high-static low-dynamic stiffness (HSLDS) vibration isolator was proposed by Zhou and Liu (2010). The tunable semi-active control system was connected to mechanical springs and comprised an electromagnet and a magnetic generator, and the positive and negative stiffness can be controlled. An isolation layer with a magnetorheological elastomer (MRE) was developed, where the material stiffness can be changed via electrical current (Du *et al.* 2011). The experimental results revealed that the acceleration can be controlled effectively through a semi-active configuration.

A semi-active isolation mechanism called a leverage-type stiffness-controllable isolation system (LSCIS) was proposed by Lu *et al*. (2011). The stiffness of the isolation layer can be altered instantaneously by switching the pivot point of the lever arm, thereby achieving control of the structure. A control algorithm named the least input energy method (LIEM) was then proposed by Lu *et al.* (2012). A series of shaking table tests indicated that displacement and acceleration responses can be reliably ameliorated. Nevertheless, in these early studies of the LSCIS, excessive displacement of the isolation layer was sporadically observed under near-fault earthquakes, which may endanger the isolation system. To alleviate this problem, an algorithm that considers the minimum energy combination of the kinetic and potential energy is proposed here.

The remainder of this study is structured as follows. The mechanism of the LSCIS and the proposed minimal energy weighting (MEW) method are presented in Sections 2 and 3, respectively. Numerical simulations for MEW parameter optimization and performance evaluation using various earthquakes are given in Section 4. The experimental results from a series of shaking table tests are presented in Section 5. The conclusions are given in Section 6.

2. Minimal energy weighting method

For an adaptive stiffness control system, the controllable stiffness $k_r(t)$, which can be tuned between 0 and the upper bound $k_{r,max}$, can be divided into an uncontrollable stiffness k_{r0} and a variable stiffness $\Delta k_r(t)$, expressed as

$$k_r(t) = k_{r0} + \Delta k_r(t) \tag{1}$$

The equation of motion can be rewritten using the state space method (Naeim and Kelly 1999) as

$$\dot{\mathbf{z}}(t) = \mathbf{A}\mathbf{z}(t) + \mathbf{B}\mathbf{D}_d\mathbf{z}(t)\Delta k_r(t) + \mathbf{E}\ddot{x}_g(t) \tag{2}$$

where **z**(t) represents the state vector; **A** represents the system matrix; **B** represents the support matrix, and **E** represents the excitation matrix. The system matrix can be expressed as

$$\mathbf{A}=\mathbf{z}(\mathrm{t})=\begin{Bmatrix}\dot{\mathrm{x}}_{\mathrm{s}}(\mathrm{t})\\ \dot{\mathrm{x}}_{\mathrm{b}}(\mathrm{t})\\ \mathrm{x}_{\mathrm{s}}(\mathrm{t})\\ \mathrm{x}_{\mathrm{b}}(\mathrm{t})\end{Bmatrix}\quad \mathbf{B}=\begin{Bmatrix}0\\ -1/m_b\\ 0\\ 0\end{Bmatrix}\quad \mathbf{E}=\begin{Bmatrix}-1\\ -1\\ 0\\ 0\end{Bmatrix} \tag{3}$$

The mass **M**, damping **C**, and stiffness **K** of the isolated structure are expressed as

$$\mathbf{M}=\begin{bmatrix}m_s & 0\\ 0 & m_b\end{bmatrix}\quad \mathbf{K}=\begin{bmatrix}k_s & -k_s\\ -k_s & k_s+k_{r0}\end{bmatrix}$$
$$\mathbf{C}=\begin{bmatrix}c_s & -c_s\\ -c_s & c_s+c_r\end{bmatrix}\quad \mathbf{D}_{\mathrm{d}}=\begin{bmatrix}0 & 0 & 0 & 1\end{bmatrix} \tag{4}$$

where m_s and m_b are the masses of the main structure and the isolation layer, and k_s and $c_s$are the stiffness and damping coefficient of the superstructure; $\ddot{x}_g(t)$ denotes the earthquake acceleration; $x_s(t)$ and $x_b(t)$ represents the relative displacement of the main structure and the isolation layer, respectively.

The discreet state space equation can be further derived as

$$\mathbf{z}[k+1]=\mathbf{A}_d\mathbf{z}[k]+\mathbf{B}_d\mathbf{D}_d\mathbf{z}[k]\Delta k_r[k]+\mathbf{E}_d\ddot{x}_g[k] \tag{5}$$

$$\begin{aligned}\mathbf{A}_d &= e^{\mathbf{A}\Delta t}\\ \mathbf{B}_d &= \mathbf{A}^{-1}(\mathbf{A}_d-\mathbf{I})\mathbf{B}\\ \mathbf{E}_d &= \mathbf{A}^{-1}(\mathbf{A}_d-\mathbf{I})\mathbf{E}\end{aligned} \tag{6}$$

where $\mathbf{A}_{\mathrm{d}}$, $\mathbf{B}_{\mathrm{d}}$, and $\mathbf{E}_{\mathrm{d}}$ are the discrete forms of **A**, **B**, and **E**, and $\mathbf{z}[k+1]$ is the state space response in time step (k + 1), which can be determined from the structural responses $\mathbf{z}[k]$, $\ddot{x}_g[k]$, and $\Delta k_r[k]$; $\ddot{x}_g[k]$ is the ground acceleration.

As demonstrated in previous studies, the superstructure response can be ameliorated by the LIEM under most far-field earthquakes (Naeim and Kelly 1999). Nevertheless, extreme displacement may occur on the isolation layer under near-fault earthquakes. To resolve this, an algorithm called MEW is proposed. By applying the MEW algorithm, the overall structural energy, including the potential and kinetic energy, can be minimized under external vibration.

To derive the optimal $\Delta k_r[k]$ Eq. (5) is rewritten as

$$\mathbf{z}[k+1]=\mathbf{A}_{\mathrm{d}}\mathbf{z}[k]+\Delta k_r[k]\mathbf{B}_{1d}\mathbf{z}[k]+\mathbf{E}_d\ddot{x}_g[k] \quad (7)$$

where

$$\mathbf{B}_{1d}=\mathbf{B}_d\mathbf{D}_d \quad (8)$$

The kinetic energy can be stated as

$$E_k[k+1]=\frac{1}{2}\left(a_1[k]\right)\Delta k_r[k]^2+a_2[k]\Delta k_r[k]+a_3[k] \quad (9)$$

where

$$a_1[k]=\mathbf{z}[k]^{\mathrm{T}}\mathbf{B}_{1\mathrm{d}}{}^{\mathrm{T}}\mathbf{D}_2{}^{\mathrm{T}}\mathbf{M}\mathbf{D}_2\mathbf{B}_{1\mathrm{d}}\mathbf{z}[k] \quad (10)$$

$$a_2[k]=\mathbf{z}[k]^{\mathrm{T}}\mathbf{B}_{1\mathrm{d}}{}^{\mathrm{T}}\mathbf{D}_2{}^{\mathrm{T}}\mathbf{M}\mathbf{D}_2\left(\mathbf{A}_d\mathbf{z}[k]+\mathbf{E}_{\mathrm{d}}\ddot{x}_g[k]\right)+\mathbf{D}\mathbf{M}\mathbf{D}_2\mathbf{B}_{1\mathrm{d}}\mathbf{z}[k]\dot{x}_g[k] \quad (11)$$

$$a_3[k]=\frac{1}{2}\left(\mathbf{z}[k]^{\mathrm{T}}\mathbf{A}_d{}^{\mathrm{T}}+\mathbf{E}_d{}^{\mathrm{T}}\ddot{x}_g[k]\right)\mathbf{D}_2{}^{\mathrm{T}}\mathbf{M}\mathbf{D}_2\left(\mathbf{A}_{\mathrm{d}}\mathbf{z}[k]+\mathbf{E}_{\mathrm{d}}\ddot{x}_g[k]\right) \quad (12)$$

$$+\mathbf{D}\mathbf{M}\mathbf{D}_2\left(\mathbf{A}_d\mathbf{z}[k]+\mathbf{E}_{\mathrm{d}}\ddot{x}_g[k]\right)\dot{x}_g[k]+\frac{1}{2}\mathbf{D}\mathbf{M}\mathbf{D}^{\mathrm{T}}\left(\dot{x}_g[k]\right)^2$$

$$\mathbf{D}=\begin{bmatrix}1 & 1\end{bmatrix},\ \mathbf{D}_2=\begin{bmatrix}1 & 0 & 0 & 0\\ 0 & 1 & 0 & 0\end{bmatrix} \quad (13)$$

The potential energy of the superstructure $E_{p,sup}[k+1]$, and the potential energy of the isolation layer $E_{p,iso}[k+1]$ are written as

$$E_{p,sup}[k+1]+E_{p,iso}[k+1]=\frac{1}{2}(k_s)\times(x_s[k+1])^2+\frac{1}{2}(\Delta K_r+K_{r0})\times(x_b[k+1])^2$$

$$=\frac{1}{2}\left(b_{1,sup}[k]+b_{1,iso}[k]\right)\Delta k_r[k]^2+\left(b_{2,sup}[k]+b_{2,iso}[k]\right)\Delta k_r[k]+\left(b_{3,sup}[k]+b_{3,iso}[k]\right) \quad (14)$$

where

$$b_{1,iso}[k]=0.5(\mathbf{B}_{1dL}\mathbf{z}[k])^2 \quad (15)$$

$$b_{2,iso}[k]=\mathbf{B}_{1dL}\mathbf{z}[k](\mathbf{A}_{dL}\mathbf{z}[k]+\mathbf{E}_{dL}\ddot{x}_g[k])K_{r0} \quad (16)$$

$$b_{3,iso}[k]=0.5(\mathbf{A}_{dL}\mathbf{z}[k])^2K_{r0}+0.5\left(\mathbf{E}_{dL}\ddot{x}_g[k]\right)K_{r0}+\mathbf{A}_{dL}\mathbf{z}[k]\mathbf{E}_{dL}\ddot{x}_g[k]K_{r0} \quad (17)$$

$$b_{1,sup}[k]=0.5k_s\left((\mathbf{B}_{1dT}\mathbf{z}[k])^2+(\mathbf{B}_{1dL}\mathbf{z}[k])^2-2\mathbf{B}_{1dT}\mathbf{z}[k]\mathbf{B}_{1dL}\mathbf{z}[k]\right) \quad (18)$$

$$b_{2,sup}[k]=\mathbf{B}_{1dL}\mathbf{z}[k]\Delta K_r\left(2\left(\mathbf{A}_{dL}\mathbf{z}[k]+\mathbf{E}_{dL}\ddot{x}_g[k]\right)+\left(\mathbf{A}_{dT}\mathbf{z}[k]+\mathbf{E}_{dT}\mathbf{z}[k]\right)\right)$$

$$+\mathbf{B}_{1dT}\mathbf{z}[k]\Delta K_r\left(2\left(\mathbf{A}_{dT}\mathbf{z}[k]+\mathbf{E}_{dT}\ddot{x}_g[k]\right)+\left(\mathbf{A}_{dL}\mathbf{z}[k]+\mathbf{E}_{dL}\mathbf{z}[k]\right)\right) \quad (19)$$

$$b_{3,sup}[k]=0.5(\mathbf{A}_{dL}\mathbf{z}[k])^2k_s+0.5\left(\mathbf{E}_{dL}\ddot{x}_g[k]\right)k_s+\mathbf{A}_{dL}\mathbf{z}[k]\mathbf{E}_{dL}\ddot{x}_g[k]k_s$$

$$+0.5(\mathbf{A}_{dT}\mathbf{z}[k])^2k_s+0.5\left(\mathbf{E}_{dT}\ddot{x}_g[k]\right)k_s+\mathbf{A}_{dT}\mathbf{z}[k]\mathbf{E}_{dT}\ddot{x}_g[k]k_s$$

$$-0.5\mathbf{A}_{dT}\mathbf{z}[k]\mathbf{A}_{dL}\mathbf{z}[k]k_s-0.5\mathbf{E}_{dT}\ddot{x}_g[k]\mathbf{E}_{dL}\ddot{x}_g[k]k_s$$

$$-0.5\mathbf{A}_{dT}\mathbf{z}[k]\mathbf{E}_{dL}\ddot{x}_g[k]k_s-0.5\mathbf{A}_{dL}\mathbf{z}[k]\mathbf{E}_{dT}\ddot{x}_g[k]k_s \quad (20)$$

To determine the optimal stiffness increment, the energy performance index $J[k+1]$ is proposed as

$$J[k+1]=E_k[k+1]+\frac{R}{2}\Delta k_r[k]^2+QE_p\times E_{p,sup}[k+1]+QE_p\times E_{p,iso}[k+1] \quad (21)$$

where R is the penalty weighting of the pivot point and QE_p is the weighting of the potential energy. In Eq. (14), is simplified to accelerate the search process.

To derive the optimal $\Delta k_{r,opt}[k]$ for the minimal performance index $J[k+1]$, Eq. (21) is differentiated and set as zero

$$\frac{d\left(J[k+1]\right)}{d\left(\Delta k_r[k]\right)}=\left(a_1[k]+R\right)\Delta k_r[k]+a_2[k]=0 \quad (22)$$

The details can be derived as

$$\left(a_1+R+QE_p\times b_{2,str}+QE_p\times b_{2,iso}\right)\Delta k_r+\left(a_2+QE_p\times b_{2,str}+QE_p\times b_{2,iso}\right)=0 \quad (23)$$

The optimal stiffness increment $\Delta k_{r,opt}[k]$ can be expressed as

$$\Delta k_{r,opt}[k]=\frac{-\left(a_2+QE_p\times b_{2,str}+QE_p\times b_{2,iso}\right)}{a_1+R+QE_p\times b_{2,str}+QE_p\times b_{2,iso}} \quad (24)$$

In order to achieve adaptive stiffness control, the LSCIS is adopted in this study. The mechanism of the adaptive stiffness control system of the LSCIS is illustrated in Figs. 1(a) and 1(b), and the mathematical model is depicted in Fig. 1(c). The relationship between $\Delta k_r[k]$ and $x_p[k]$ for the LSCIS system can be expressed as

$$\Delta k_r[k]=\left[\frac{2Lx_p[k]}{(0.5L-x_p[k])^2}\right]k_{r0} \quad (25)$$

As shown in Eq. (25), a controllable $\Delta k_r[k]$ in the isolation layer is generated by properly shifting the leverage point $x_p[k]$ between $0.0202L$ and $-0.191L$ with leverage length L.

3. Numerical evaluation of proposed algorithm

3.1 Input earthquakes and numerical model

Three earthquake records with various dynamic characteristics shown in Figure 2 were applied in the numerical simulation:

(i) El Centro (S00E) earthquake; May 18, 1940; peak acceleration: 341.0 cm/s^2.

(ii) Imperial Valley (El Centro Array 6) earthquake; Channel 1 230deg; October 15, 1979; peak acceleration: 428.1 cm/s^2.

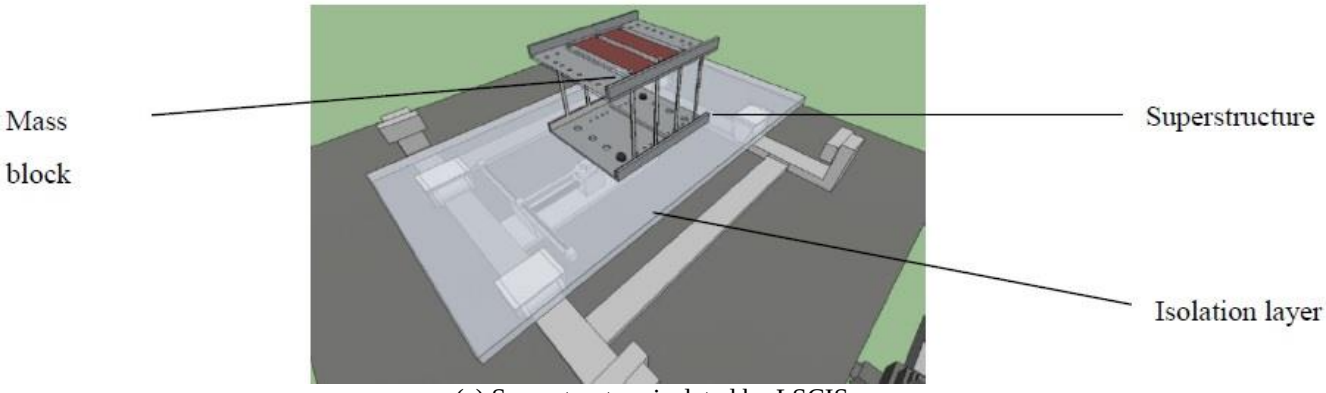

(a) Superstructure isolated by LSCIS

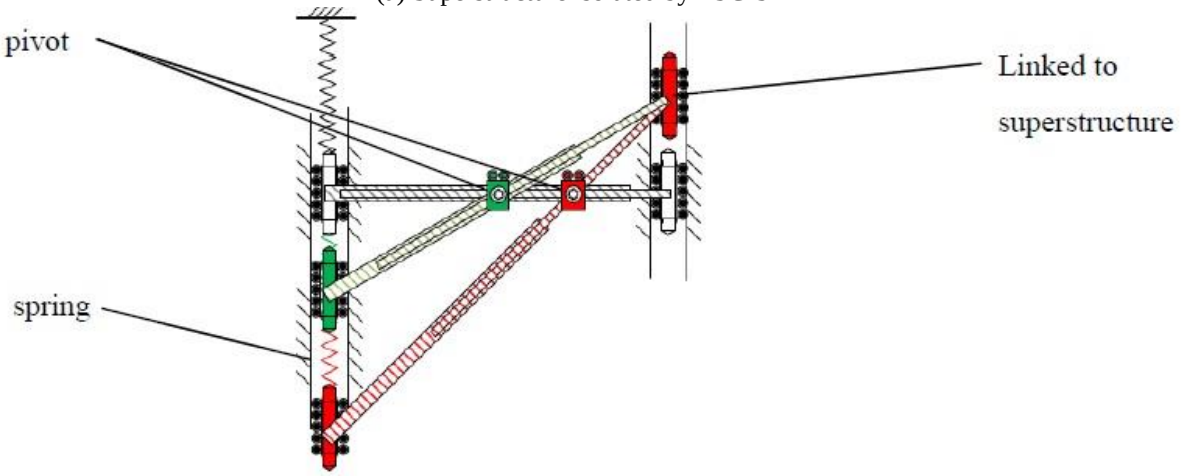

(b) Leverage mechanism

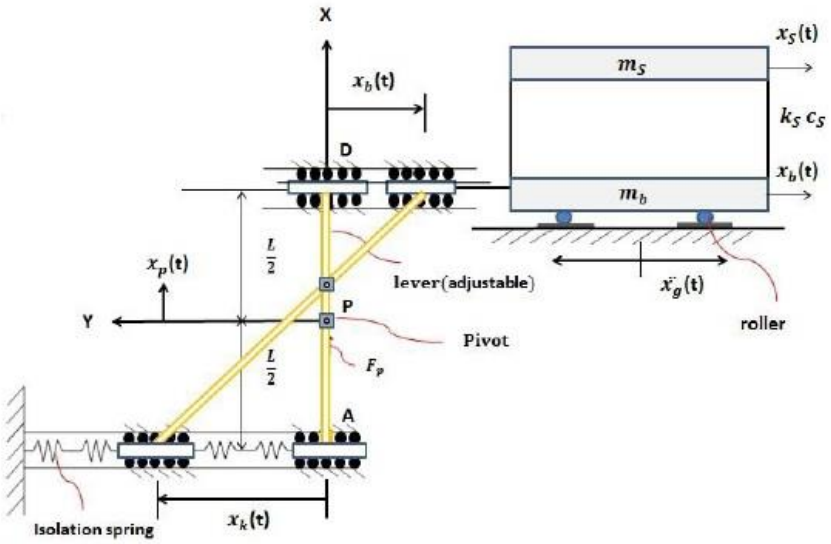

(c) Physical model for LSCIS-isolated structure

Fig. 1 The LSCIS system

(iii) Chi-Chi earthquake, Taiwan; September 20, 1999; station: TCU068 – N; peak acceleration: 0.462 g.

An 18.66-kg superstructure and a 28.30-kg isolation base were used. The practical system parameters were first identified under white-noise excitation of 0.1-g peak ground acceleration (PGA); they are listed in Table 1. The 1940 El Centro earthquake (PGA: 0.3 g) was then used to examine the identification performance. The numerical simulation was compared with the experimental results. As illustrated in Fig. 3, the actual structural behavior is reflected consistently by the identified parameters.

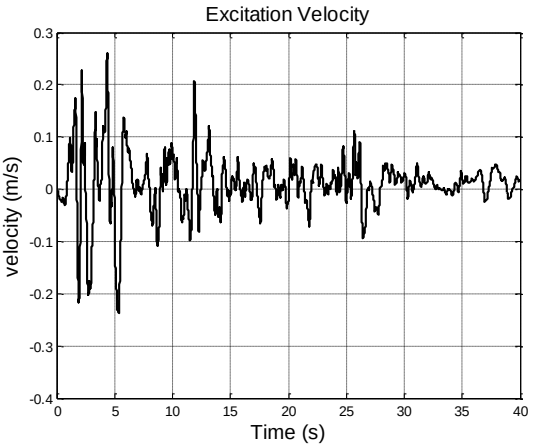

(a) Velocity (El Centro)

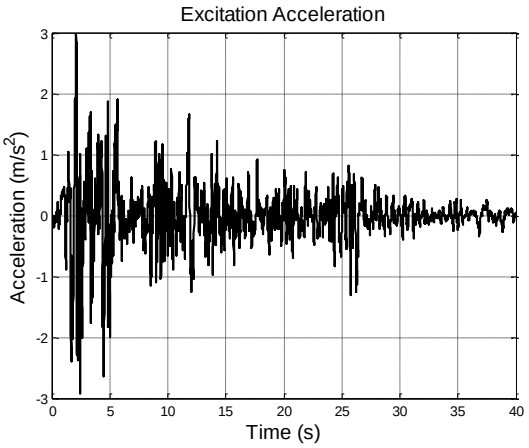

(b) Acceleration (El Centro)

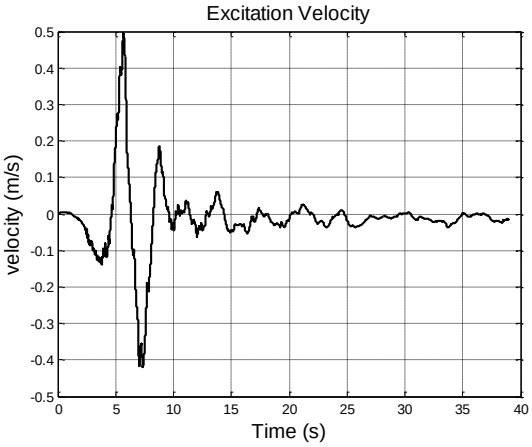

(c) Velocity (Imperial Valley)

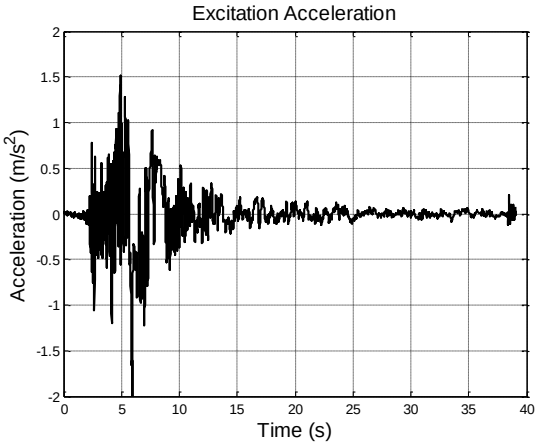

(d) Acceleration (Imperial Valley)

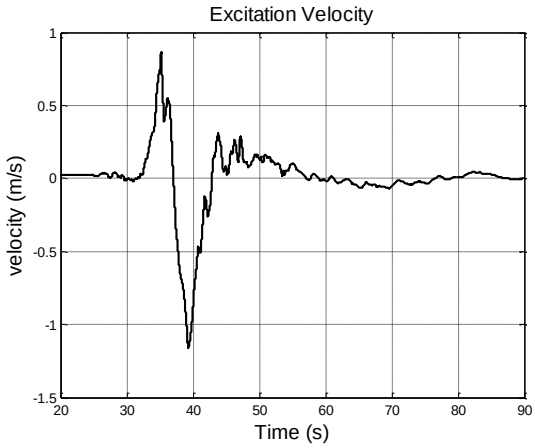

(e) Velocity (TCU-068NS)

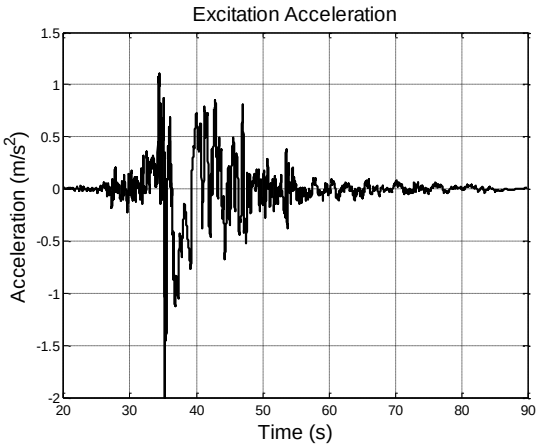

(f) Acceleration (TCU-068NS)

Fig. 2 Earthquake input for numerical simulation

Table 1 Identified parameters for the isolated system

System	Item	Value
Superstructure	Mass (m_s)	18.66kg
	Damping ratio (ξ)	0.02
	Stiffness (k_s)	2780 N/m
	Natural frequency	1.95 Hz
Isolation layer	Mass (m_b)	28.30 kg
	Isolation period (T_{r0})	2.49 s
	Damping Ratio (ξ_s)	0.075
	Stiffness (k_{r0})	300 N/m

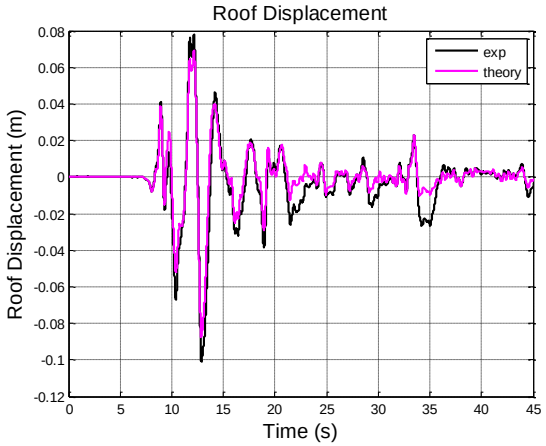

(a) Superstructure displacement

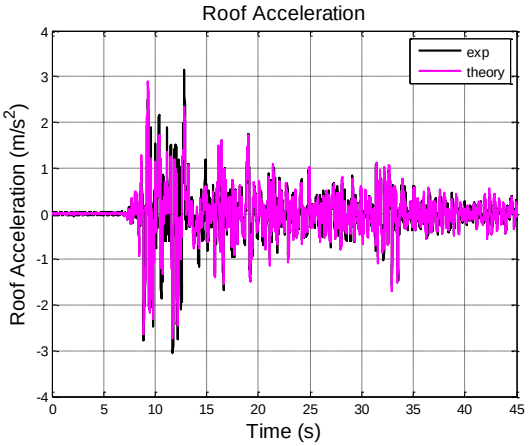

(b) Superstructure acceleration

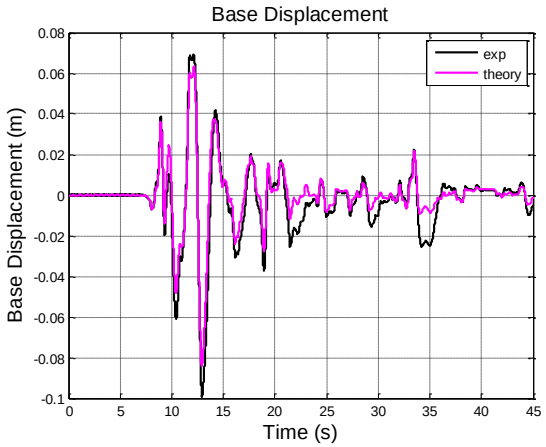

(c) Isolation layer displacement

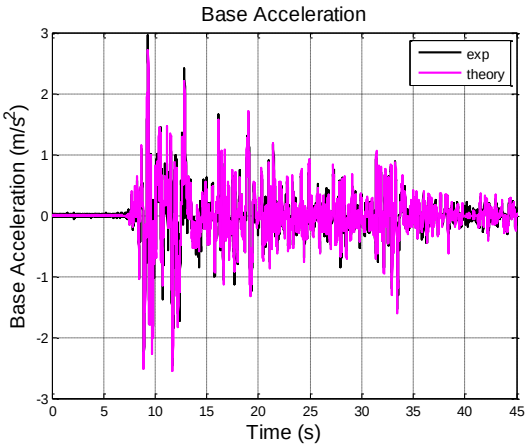

(d) Isolation layer acceleration

Fig. 3 Verification of numerical model

3.2 Control weighting optimization

Based on the identified model, the optimal control weightings were found by exciting the structure with the El Centro and Imperial Valley earthquake time histories, which are typical far-filed and near-fault earthquakes, respectively. The contour of the relative displacement and absolute acceleration under various R and QE_p values were generated and compared for the optimal arrangement. The R was set from 10^{-12} to 10^{0} and QE_p was explored from 0 to 200.

The numerical structural response under the El Centro earthquake (PGA: 0.3 g), representing a characteristic far-field earthquake, is shown on the left side of Fig. 4. As indicated, the absolute acceleration illustrated in Fig. 4(a) is exaggerated dramatically with increases of R and QE_p. Moreover, the minimum relative displacement illustrated in Fig. 4(c) can be reached through the settings 10^{-8} and 30 for R and QE_p, respectively. As both the absolute acceleration and relative displacement can be alleviated most among the searching contour, the optimum weightings of QE_p and R are determined as 30 and 10^{-8}, respectively.

The numerical simulation under the Imperial Valley earthquake (PGA: 0.2 g), reflecting the classical near-fault characteristic, is illustrated on the right side of Fig. 4.

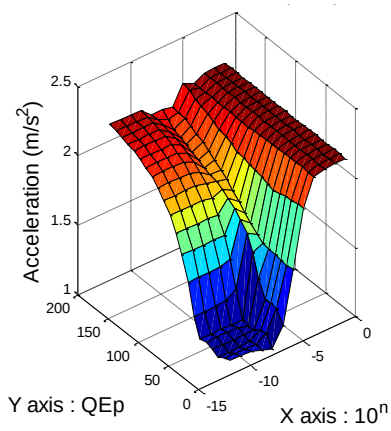

(a) Superstructure acceleration (El Centro PGA = 0.3 g)

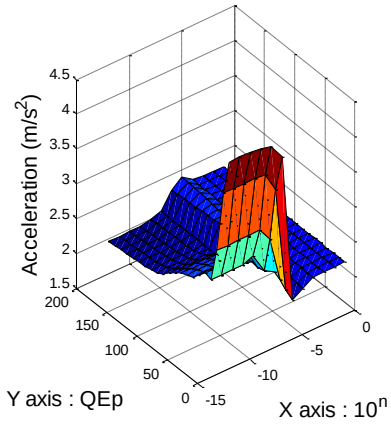

(b) Superstructure acceleration (Imperial Valley PGA = 0.3 g)

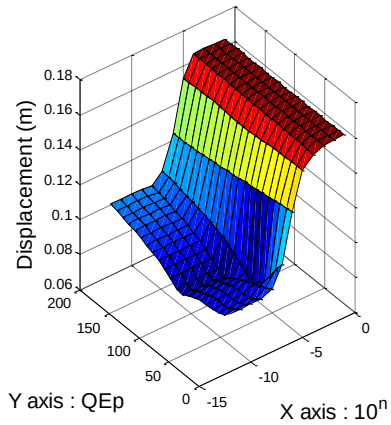

(c) Isolation layer displacement (El Centro PGA = 0.3 g)

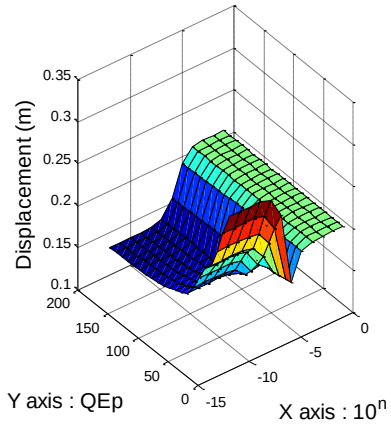

(d) Isolation layer displacement (Imperial Valley PGA = 0.3 g)

Fig. 4 Control parameter optimization

The relative displacement is amplified when QE_p approaches 0 and R is lower than 10^{-7}. In comparison to the LIEM control ($QE_p = 0$、 $R = 10^{-8}$), the displacement response can be significantly suppressed when QE_p is set as 30. Thus, the minimum displacement is reached through the setting of QE_p = 180 and R= 10^{-8}. For the acceleration response, the minimum acceleration of the superstructure is achieved with $QE_p = 0$ and $R = 10^{-6}$. As relative displacement is the main concern under near-fault earthquake, and similar displacement can be achieved by the setting of $QE_p = 180$ and $R = 10^{-8}$, the optimal weightings are set as $QE_p = 180$ and $R = 10^{-8}$ for near-fault earthquakes.

Based on the results, R is determined as 10^{-8}. Two types of MEW control algorithm with different QE_p values are proposed in accordance with various earthquake characteristics. The near-fault MEW control ($QE_p = 180$) is considered for near-fault earthquakes to reduce the extreme displacements; and the generic MEW control, where QE_p = 30, is proposed for common earthquakes. Although an optimal response reduction cannot be obtained using the generic MEW control under near-fault earthquakes, improvements in control efficiency are expected after the appropriate consideration of the potential energy. Depending on the seismic zone of the structure's location, the optimal algorithm can be selected. For example, the generic MEW control can be deployed outside near-fault areas. The near-fault MEW control can be adopted when structures are located inside the near-fault zone.

3.3 Structural response under earthquake conditions

The structural responses of several algorithms, including passive, LIEM, generic MEW, and near-fault MEW control, under diverse earthquake excitations were evaluated. For the passive control case, the LSCIS pivot point was kept constant in the center, and thus the value of the isolation stiffness remained as the original stiffness K_{r0}, with no stiffness increment throughout the excitation. Although better acceleration performance can be achieved by extending the isolation period, excessive displacement of the isolation layer under near-fault earthquakes hinders the practicality of the long-period isolation system. In contrast, with the reduction in displacement, the acceleration is largely influenced by a relatively small isolation period. Since the isolation period is commonly suggested to be between 2 and 3 s (Naeim and Kelly 1999), the isolation

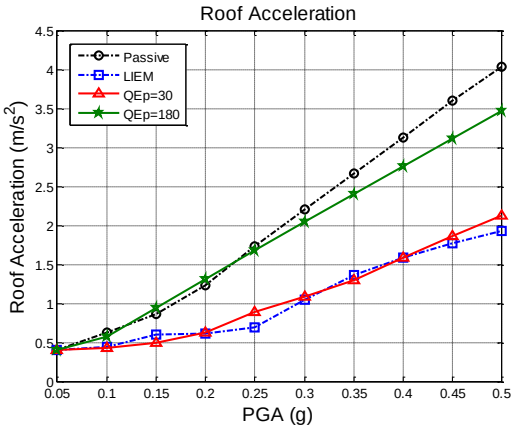

(a) Superstructure acceleration (El Centro)

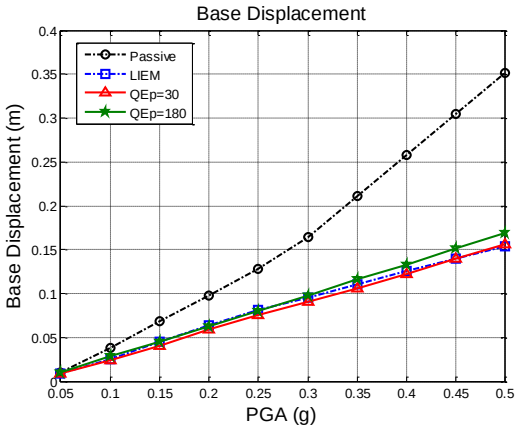

(b) Isolation layer displacement (El Centro)

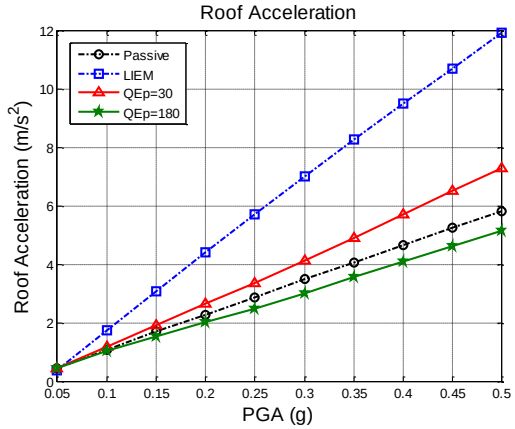

(c) Superstructure acceleration (Imperial Valley)

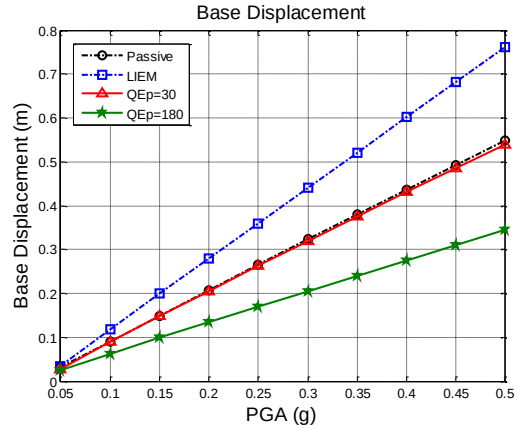

(d) Isolation layer displacement (Imperial Valley)

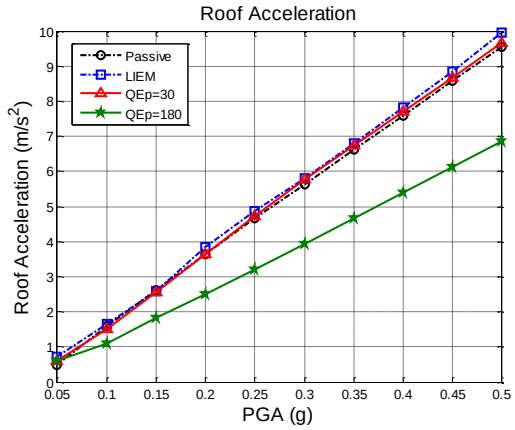

(e) Superstructure acceleration (TCU-068NS)

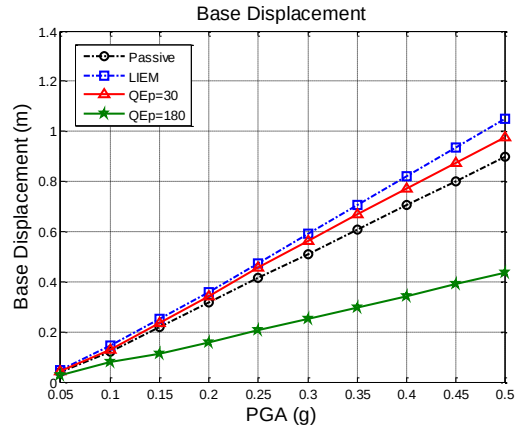

(f) Isolation layer displacement (TCU-068NS)

Fig. 5 Numerical simulation of passive, LIEM, generic MEW (QEp=30), and near-fault MEW (QEp=180)

period of the structure was set as 2.5 s. Moreover, the control parameters QE_p and R of the LIEM method were set as 0 and 10^{-8}, respectively.

The superstructure acceleration under the El Centro earthquake with numerous earthquake intensities is illustrated in Fig. 5(a). Among the four control modes, the generic MEW control has the most efficient performance for the far-field earthquake. Generic MEW control and the LIEM have similar responses for PGA values of 0.25, 0.45, and 0.5 g; satisfactory control effectiveness is achieved for PGA values of 0.3 and 0.4 g. Regarding the near-fault MEW control, greater responses are observed for PGA values of 0.15 and 0.2 g compared with those for the passive control; nevertheless, the acceleration responses at 0.25 and 0.5 g are smaller than those of the passive control algorithm. The displacements of the isolation layer under the El Centro earthquake with various magnitudes are illustrated in Fig. 5(b). The generic and near-fault MEW control modes both display better control effects for all PGA values compared to those of the LIEM control algorithm. To conduct a detailed comparison, the structural responses under the El Centro earthquake (PGA: 0.3 g) are

Table 2 Simulated peak response under El Centro earthquake (PGA=0.3 g)

Control system	Superstructure displacement (m)	Isolation layer displacement (m)	Superstructure acceleration (m/s^2)	Isolation layer acceleration (m/s^2)
Passive	0.174	0.164	2.176	1.753
	(1.00)	(1.00)	(1.00)	(1.00)
LIEM	0.093	0.095	1.050	0.873
($R=10^{-8}$)	(0.534)	(0.579)	(0.482)	(0.498)
LIEM+Ep	0.091	0.090	1.083	0.889
(QEp=30)	(0.523)	(0.548)	(0.497)	(0.507)
LIEM+Ep	0.109	0.098	2.040	1.532
(QEp=180)	(0.626)	(0.597)	(0.933)	(0.873)

Note: numbers in parentheses represent ratio between passive and controlled responses

Table 3 Simulated peak response under Imperial Valley earthquake (PGA=0.2 g)

Control system	Superstructure displacement (m)	Isolation layer displacement (m)	Superstructure acceleration (m/s^2)	Isolation layer acceleration (m/s^2)
Passive	0.222	0.208	2.269	1.985
	(1.00)	(1.00)	(1.00)	(1.00)
LIEM	0.277	0.280	4.417	2.557
($R=10^{-8}$)	(1.247)	(1.346)	(1.946)	(1.288)
LIEM+Ep	0.209	0.205	2.634	2.425
(QEp=30)	(0.941)	(0.985)	(1.16)	(1.221)
LIEM+Ep	0.145	0.134	2.008	2.188
(QEp=180)	(0.653)	(0.644)	(0.884)	(1.102)

Note: numbers in parentheses represent ratio between passive and controlled responses

listed in Table 2. The maximum displacements of the isolation layer for the passive, LIEM, generic MEW, and near-fault MEW control are 0.164 (100%), 0.095 (57.9%), 0.090 (54.8%), and 0.098 (59.7%) m, respectively. The maximum superstructure accelerations for the four control modes are 2.176 (100%), 1.050 (48.2%), 1.083 (49.7%), and 2.040 (93.3%) m/s^2, respectively. As both displacement and acceleration can be reduced, the advantage of considering the potential energy under far-field earthquakes is verified.

The superstructure absolute accelerations under the Imperial Valley earthquake with various magnitudes are illustrated in Fig. 5(c). Compared to those observed for the passive control, the acceleration responses observed for the near-fault MEW control are smaller for PGA values exceeding 0.2 g. Although both the LIEM and generic MEW control yield greater responses for all PGAs compared with those of the passive control algorithm, the response enlargement for the generic MEW control is noticeably smaller than that for the LIEM control algorithm.

The displacement levels of the isolation layer under the Imperial Valley earthquake with various magnitudes are illustrated in Fig. 5(d). The near-fault MEW control exhibits the most effective control for earthquakes above 0.2 g, representing a significant improvement over the LIEM. The detailed responses of the four control modes under the Imperial Valley earthquake (PGA: 0.2 g) are listed in Table 3. As indicated, the maximum displacements of the isolation layer determined for the passive, LIEM, generic, and near-fault control are 0.208 (100%), 0.280 (134.6%), 0.205 (98.5%), and 0.134 (64.4%) m, respectively. The maximum superstructure accelerations for the passive, LIEM, generic MEW, and near-fault MEW control modes for a PGA value of 0.2 g are 2.269 (100%), 4.417 (194.6%), 2.634 (116%), and 2.008 (88.4%) m/s^2, respectively. With the relative displacement of the isolation layer largely ameliorated, the superior performance of the near-fault MEW control is demonstrated.

As the main objective of the present study is to control the excessive displacement of the isolation layer under near-fault earthquakes, the typical near-fault TCU-068NS

Table 4 Simulated peak response under Chi-Chi TCU-068NS earthquake (PGA=0.2 g)

Control system	Superstructure displacement (m)	Isolation layer displacement (m)	Superstructure acceleration (m/s^2)	Isolation layer acceleration (m/s^2)
Passive	0.340	0.317	3.659	3.039
	(1.00)	(1.00)	(1.00)	(1.00)
LIEM	0.367	0.359	3.815	3.778
($R=10^{-8}$)	(1.079)	(1.132)	(1.042)	(1.243)
LIEM+Ep	0.346	0.341	3.627	3.482
(QEp=30)	(1.017)	(1.075)	(0.991)	(1.145)
LIEM+Ep	0.172	0.159	2.512	2.632
(QEp=180)	(0.505)	(0.501)	(0.686)	(0.866)

Note: numbers in parentheses represent ratio between passive and controlled responses

earthquake was used for verification. Figs. 5(e) and 5(f) present the absolute superstructure accelerations and relative isolation layer displacements for various PGA values, respectively. The near-fault control algorithm yields the smallest response for the various PGA values. For earthquakes exceeding 0.2 g, the displacement of the isolation layer can be significantly suppressed by the near-fault MEW control algorithm. The structural responses for a PGA value of 0.2 g are further detailed in Table 4. As shown in this table, the maximum accelerations of the superstructure for the passive, LIEM, generic MEW, and near-fault MEW control modes are 3.659 (100%), 3.815 (104.2%), 3.627(99.1%), and 2.512 (68.6%) m/s2, respectively, and the maximum displacements of the isolation layer for these four control modes are 0.317 (100%), 0.359 (113.2%), 0.341 (107.5%), and 0.159 (50.1%) m, respectively. These results demonstrate that both the superstructure acceleration and isolation layer displacement can be effectively controlled by the near-fault MEW control, and better performance can also be achieved by the generic MEW control compared to the LIEM. Moreover, promising results can still be achieved when the near-fault MEW control is applied under far-field earthquakes. Compared to the passive control, an estimated 30% reduction in acceleration can be provided by the semi-active control, and similar displacement control results can be expected for the other three methods (LIEM, far-field MEW, and near-fault MEW control).

4. Experimental verification

To demonstrate the feasibility of the proposed algorithms, a series of shaking table experiments was executed. As the maximum stroke of the shaking table is limited to 12 cm, only the El Centro and Imperial Valley earthquakes were utilized as the ground input during the experiments. The experimental setup, including the control system, the lever device, experimental specimen, and the LSCIS, is shown in Figure 6. As indicated, the pivot point can be shifted between point A and D for the optimal isolation stiffness. Linear variable differential transformers (LVDTs) (± 300 and ± 100 mm), a velocity meter (± 100 kine), and an accelerometer (± 2 G) were deployed to measure structural responses.

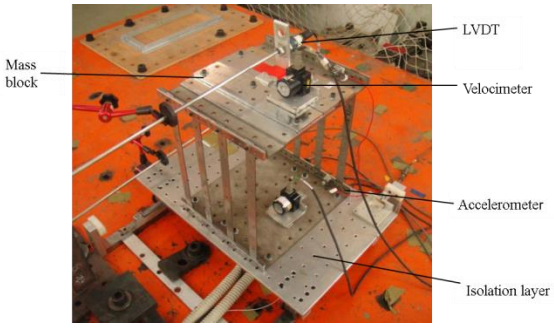

(a) Experimental specimen

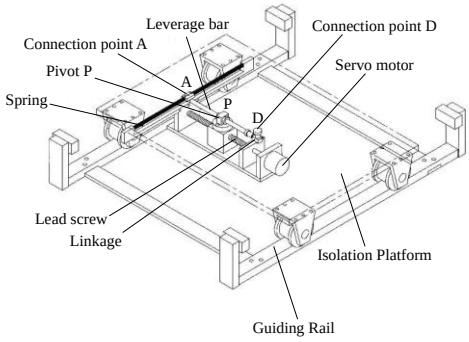

(b) lever device

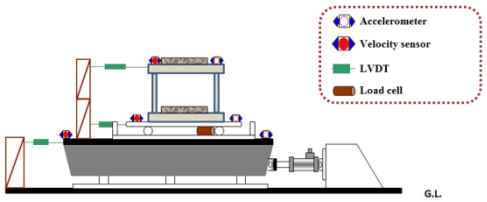

(c) instrumentation

Fig. 6 Experimental set-up of the LSCIS

Table 5 Experimental peak response under El Centro earthquake (PGA=0.3 g)

Control system	Superstructure displacement (m)	Isolation layer displacement (m)	Superstructure acceleration (m/s^2)	Isolation layer acceleration (m/s^2)
Passive	0.104	0.101	1.917	1.585
	(1.00)	(1.00)	(1.00)	(1.00)
LIEM	0.069	0.071	1.295	0.805
($R=10^{-8}$)	(0.66)	(0.70)	(0.68)	(0.51)
LIEM+Ep	0.069	0.070	0.989	1.000
(QEp=30)	(0.66)	(0.69)	(0.52)	(0.63)
LIEM+Ep	0.080	0.073	1.815	1.435
(QEp=180)	(0.77)	(0.73)	(0.95)	(0.91)

Note: numbers in parentheses represent ratio between passive and controlled responses

Table 6 Experimental peak response under Imperial Valley earthquake (PGA=0.2 g)

Control system	Superstructure displacement (m)	Isolation layer displacement (m)	Superstructure acceleration (m/s^2)	Isolation layer acceleration (m/s^2)
Passive	0.125	0.119	2.332	1.931
	(1.00)	(1.00)	(1.00)	(1.00)
LIEM	0.134	0.131	2.161	1.592
($R=10^{-8}$)	(1.07)	(1.10)	(0.93)	(0.82)
LIEM+Ep	0.108	0.102	1.899	1.111
(QEp=30)	(0.86)	(0.85)	(0.81)	(0.58)
LIEM+Ep	0.097	0.085	1.771	1.571
(QEp=180)	(0.78)	(0.71)	(0.76)	(0.81)

Note: numbers in parentheses represents ratio between passive and controlled responses

4.1 Comparison of algorithms

The structural responses under the El Centro (PGA: 0.3 g) and Imperial Valley (PGA: 0.2 g) earthquakes with various algorithms were first compared. The results of the passive, LIEM, generic MEW, and near-fault MEW control modes under the El Centro earthquake (PGA: 0.3 g) are shown in Table 5. The peak displacements of the isolation layer under the passive, LIEM, generic MEW, and near-fault MEW control were 0.101 (100%), 0.071 (70.2%), 0.070 (69.3%), and 0.073 (72.8%) m, respectively. Based on the experimental results, the displacement of the isolation layer was effectively dampened by the LIEM, generic MEW, and near-fault MEW control modes; the displacement of the isolation layer was suppressed most by the generic MEW control. Moreover, the structural accelerations were also compared. The peak superstructure accelerations for the passive, LIEM, generic MEW, and near-fault MEW control were 1.917 (100%), 1.295 (67.6%), 0.989 (51.6%), and 1.815 (94.7%) m/s^2, respectively. Among the four methods, the superstructure acceleration was controlled best by the generic MEW control, with an estimated 10% advantage over the LIEM. The performance of the near-fault MEW control is close to that of the passive control system as the near-fault MEW control is mainly considered for near-fault ground excitation.

The displacements of the isolation layer for the various algorithms under the Imperial Valley earthquake (PGA: 0.2 g) are shown in Table 6. The peak displacements of the isolation layer for the passive, LIEM, generic MEW, and near-fault MEW algorithms were 0.119 (100%), 0.131 (109.5%), 0.102 (85.3%), and 0.085 (71.3%) m, respectively. The displacement for the generic MEW and near-fault MEW control modes are depicted in Figs. 7(a) and 7(b) and Figs. 8(a) and 8(b), respectively. While the displacement of the isolation layer was significantly exaggerated under the passive and LIEM control, the maximum values for the generic MEW and near-fault MEW control modes can be effectively reduced. The near-fault MEW control exhibited optimal control under near-fault

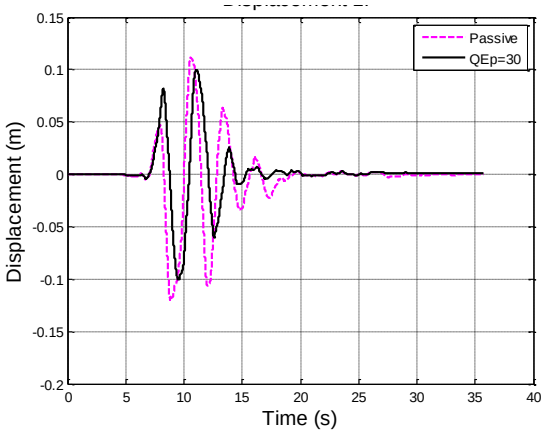

(a) Isolation layer displacement (Passive and generic MEW)

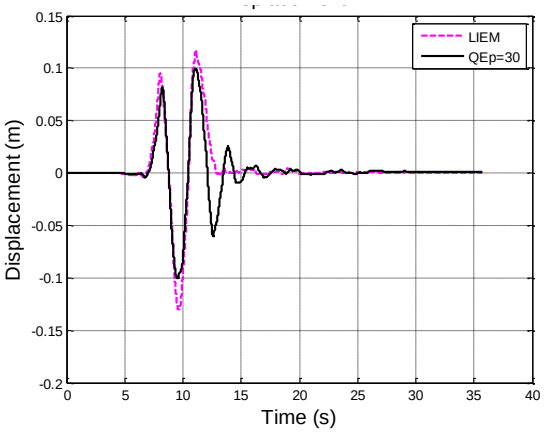

(b) Isolation layer displacement (LIEM and generic MEW)

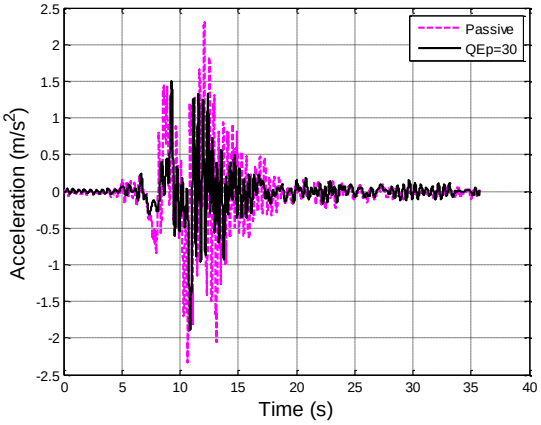

(c) Superstructure acceleration (Passive and generic MEW)

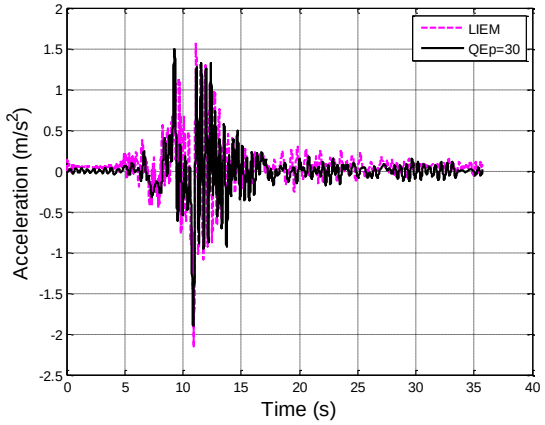

(d) Superstructure acceleration (LIEM and generic MEW)

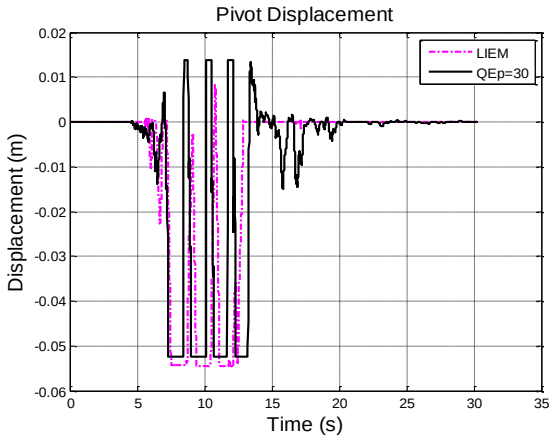

(e) Pivot displacement

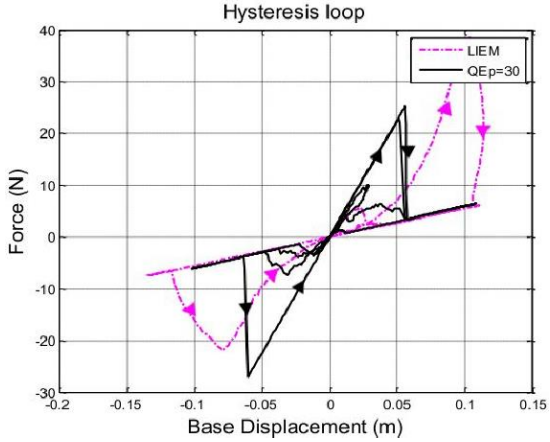

(f) Hysteresis loop

Fig. 7 Comparison of responses for passive, LIEM and generic MEW cases (Imperial Valley PGA=0.2 g)

earthquakes, demonstrating a 39% enhancement over the LIEM. The accelerations are also listed in Table 7. The peak superstructure accelerations for the passive, LIEM, generic MEW, and near-fault MEW control were 2.332 (100%), 2.161 (92.7%), 1.899 (81.4%), and 1.771 (75.9%) m/s^2, respectively. The acceleration for the generic MEW control is depicted in Figs. 7(c) and 7(d), and that for the near-fault MEW control is depicted in Figs. 8(c) and 8(d). As illustrated in these figures, the acceleration responses for peak ground excitation, occurring at 10 s, for both the generic MEW and near-fault MEW control algorithms were less than those observed for the passive and LIEM control. The acceleration for the generic MEW control algorithm was reduced by at least 10% compared with that for the LIEM control. The near-fault MEW control yielded a maximum acceleration reduction that was 17% lower than that of the LIEM.

The displacement of the pivot and the hysteresis loops of the two MEW control modes under the Imperial Valley earthquake (PGA: 0.2 g) are depicted in Figs. 7(e) and 7(f)

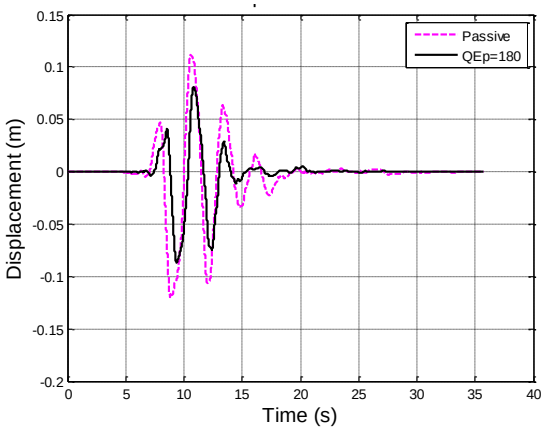

(a) Isolation layer displacement (passive and near-fault MEW)

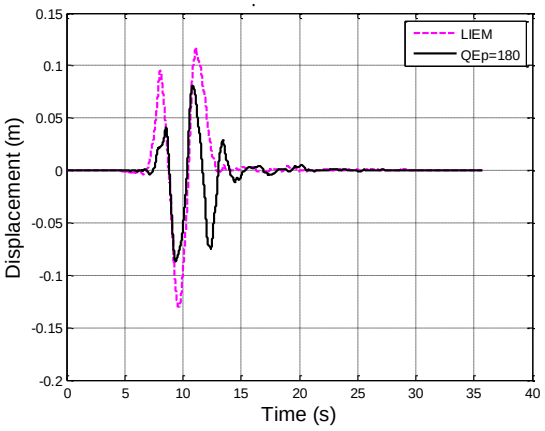

(b) Isolation layer displacement (LIEM and near-fault MEW)

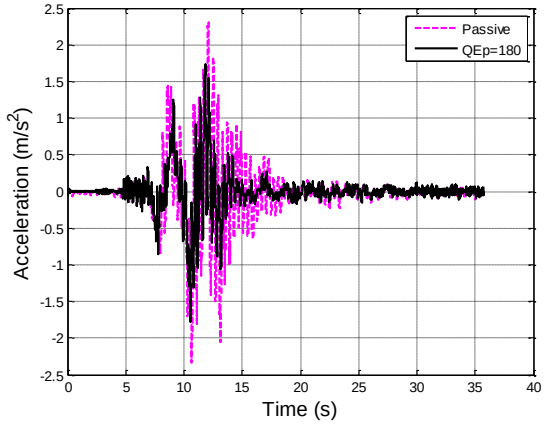

(c) Superstructure acceleration (passive and near-fault MEW)

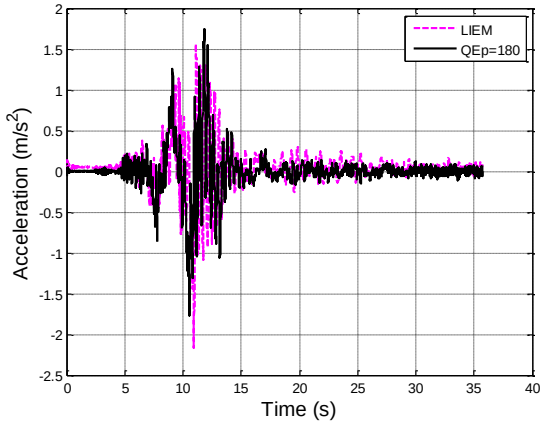

(d) Superstructure acceleration (passive and near-fault MEW)

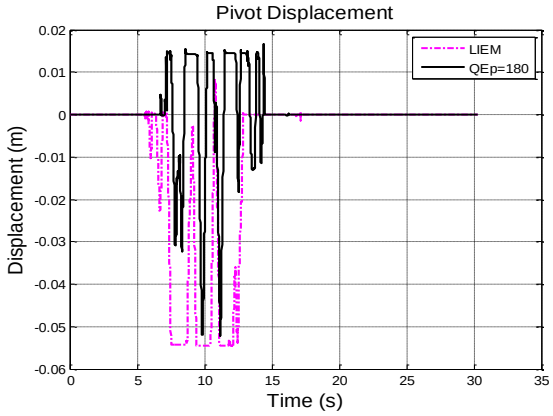

(e) Pivot displacement

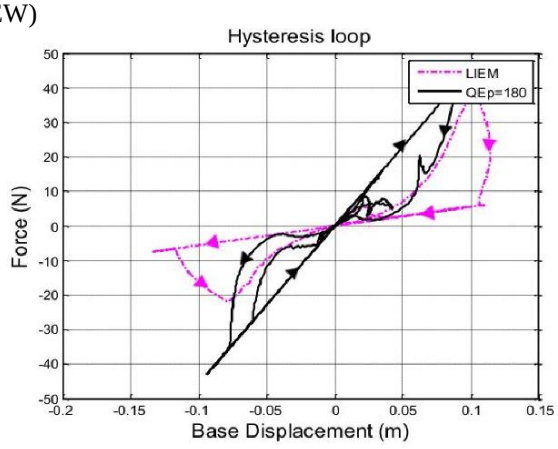

(f) Hysteresis loop

Fig. 8 Comparison of responses for passive, LIEM and near-fault MEW cases (Imperial Valley PGA=0.3 g)

and Figs. 8(e) and 8(f), respectively. The pivot displacement of the generic MEW control was controlled similarly to that of LIEM control, resulting in comparable sizes of hysteresis loops. For the near-fault MEW control, the pivot displacement was controlled toward the positive direction to provide the required damping force against the large stroke caused by the near-fault earthquake. Thus, better energy dissipation was observed from the hysteresis loop.

Moreover, the direction of hysteresis loops in both QEP and LIEM is further indicated by arrows in Figs. 7(f) and 8(f), where is clockwise in the first quadrant and counterclockwise in the fourth quadrant. The higher and lower tangents shown in the figures represent the upper and lower bounds of the isolation stiffness for the LSCIS system, which fits well with the original setting of the isolation system.

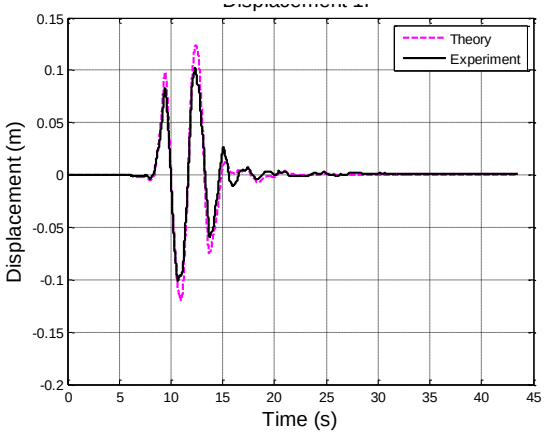

(a) Isolation layer displacement (generic MEW)

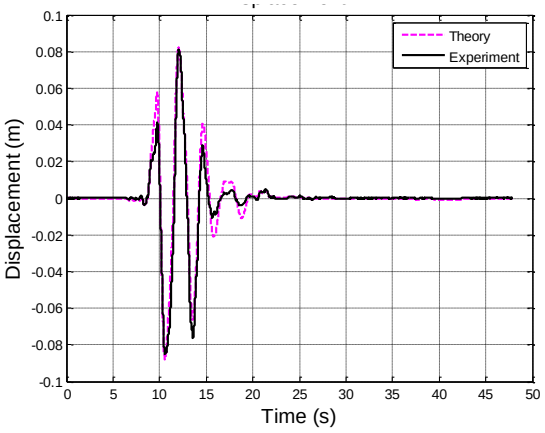

(b) Isolation layer displacement (near-fault MEW)

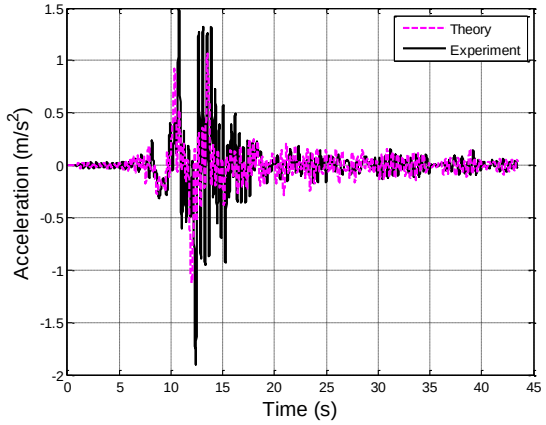

(c) Superstructure acceleration (generic MEW)

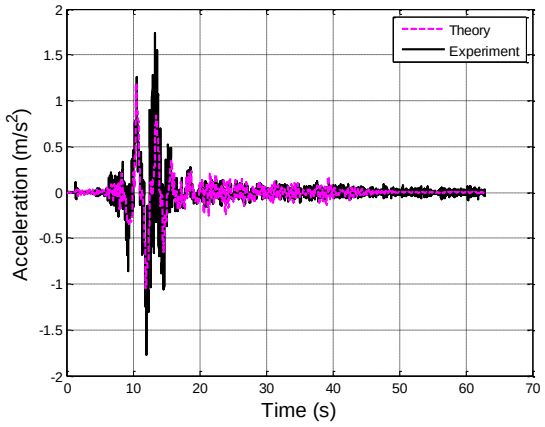

(d) Superstructure acceleration (near-fault MEW)

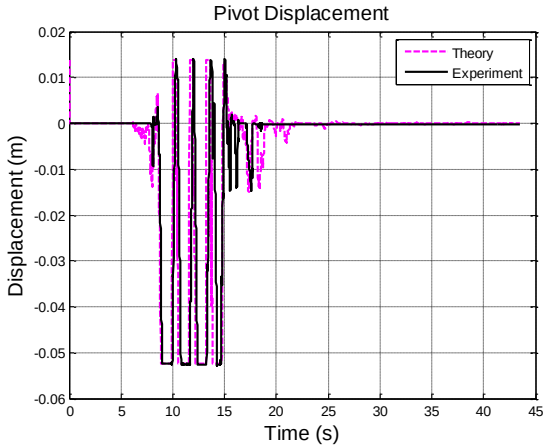

(e) Pivot displacement (generic MEW)

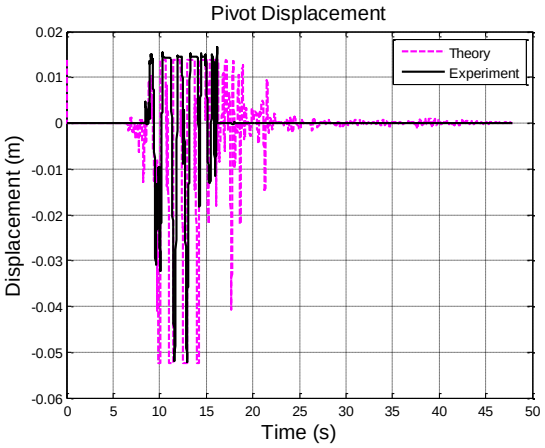

(f) Pivot displacement (near-fault MEW)

Fig. 9 Comparison between simulated and experimental responses

4.2 Comparison with theoretical analysis

To validate the implementation feasibility of the proposed semi-active control system, the Imperial Valley earthquake (PGA: 0.2 g) was used. The results from theoretical analysis and experiments were compared.

The structural response for the generic MEW control is illustrated in Figs. 9 (a), 9(c), and 9(e). As depicted, the trend of the experimental displacement response can be simulated by the theoretical analysis. As errors were generated in system parameter identification, the peak value from the theoretical analysis is slightly higher than the experimental result. Moreover, errors can be observed on the superstructure acceleration during the experiment. This may have been caused by interference from the servo motor on the accelerometer.

The structural responses for the near-fault MEW control algorithm are presented in Figs. 9(b), 9(d), and 9(f). The main tendencies from the experiment can be simulated consistently by the theoretical analysis. The experimental displacement and acceleration can be reliably estimated by

theoretical analysis. The peak experimental displacements at 11 and 13 s for the superstructure and isolation layer are precisely tracked in the numerical simulation.

5. Conclusions

To constrain the extreme displacement of isolation layers that occurs under near-fault earthquakes, the total structural energy was considered. By determining the optimum weightings between the kinetic and potential energy, two novel algorithms, namely the generic MEW and near-fault MEW control modes, were developed.

Numerical simulation shows that the generic MEW control can provide structural responses similar to those of the LIEM control under regular far-field earthquakes. The superstructure acceleration and the isolation layer displacement can be successfully ameliorated. Although the structural response may be slightly exaggerated under near-fault earthquakes, it can still be dampened more than that of the LIEM control. For the near-fault MEW control, control efficiency close to that of LIEM control can be achieved for far-field earthquakes, and control performance better than that of the passive control algorithm can be achieved. In addition, the superstructure acceleration and the displacement of the isolation layer are efficiently suppressed by the near-fault MEW control under near-fault earthquakes.

The MEW algorithms were experimentally verified through shaking table tests. Both the generic MEW and near-fault MEW control modes yield satisfactory results under near-fault earthquakes. The displacement response of the isolation layer was ameliorated successfully by the generic and near-fault MEW control. Moreover, the acceleration can be suppressed more efficiently than those under the passive control and the LIEM. The performance of the proposed system was demonstrated.

References

Anusonti-Inthra, F.G.P. (2003), "Adaptive control of semiactive variable stiffness devices for narrow-band disturbance rejection", *J. Intel. Mat. Syst. Str.*, **14**.

Battista, R.C., Carvalhob, E.M.L. and de Almeida Souza, R. (2008), "Hybrid fluid-dynamic control devices to attenuate slender structures oscillations", *Eng. Struct.*, **30**(12), 3513-3522.

Chung, L.L., Reinhorn, A.M. and Soong, T.T. (1988), "Experiments on active control of seismic structures", *J. Eng. Mech.*, **114**(2).

De la Cruz, S.T., López-Almansa, F. and Oller, S. (2007), "Numerical simulation of the seismic behavior of building structures equipped with friction energy dissipators", *Comput Struct*, **85**(1-2), 30-42.

Du, H., Li, W. and Zhang, N. (2011), "Semi-active variable stiffness vibration control of vehicle seat suspension using an MR elastomer isolator", *Smart Mater. Struct.*, **20**(10), 105003.

Lin, P.Y., Roschke, P.N. and Loh, C.H. (2007), "Hybrid controlled base-isolation with magneto-rhgeological damper and fuzzy control", *Struct. Control Health Monit.*, **14**(3), 384-405.

Lu, L.Y., Chu, S.Y., Yeh, S.W. and Chung, L.L. (2012), "Seismic test of least-input-energy control with ground velocity feedback for variable-stiffness isolation systems", *J. Sound Vib.*, **331**(4), 767-784.

Lu, L.Y., Chu, S.Y., Yeh, S.W. and Peng, C.H. (2011), "Modeling and experimental verification of a variable-stiffness isolation system using leverage mechanism", *J. Vib. Control*, **17**(12), 1869-1885.

Lu, L.Y. and Lin, G.L. (2009), "Improvement of near-fault seismic isolation using a resettable variable stiffness damper", *Eng. Struct.*, **31**(9), 2097-2114.

Martinez Rueda, J.E., (2002), "On the evolution of energy dissipation devices for seismic design", *Earthq Spectra*, **18**(2), 309-346.

Naeim, F. and Kelly, J.M. (1999), *Design of Seismic Isolated Structures*, John Wiley & Sons, Inc., New York, USA.

Narasimhan, S. and Nagarajaiah, S. (2005), "A STFT semiactive controller for base isolated buildings with variable stiffness isolation systems", *Eng. Struct.*, **27**(4), 514-523.

Nagarajaiah, S and Sahasrabudhe, S. (2006), "Seismic response control of smart sliding isolated buildings using variable stiffness systems: an experimental and numerical study", *Earthq. Eng. Struct. D.*, **35**(2), 177-197.

Shariatmadar, H. and Razavi, H.M. (2014), "Seismic control response of structures using an ATMD with fuzzy logic controller and PSO method", *Struct. Eng. Mech.*, **51**(4), 547-564.

Tamura, Y., Fujii, K., Ohtsuki, T., Wakahara, T. and Kohsaka, R. (1995), "Effectiveness of tuned liquid dampers under wind excitation", *Eng. Struct.*, **17**(9), 609-621.

Tsai, C., Chen, H.W., Hong, C.P. and Su, Y.F. (1993), "Design of steel triangular plate energy absorbers for seismic-resistant construction", *Earthq. Spectra*, **9**(3), 505-528.

Yang, J.N., Kim, J. and Agrawal, A. (2000), "Resetting semi-active stiffness damper for seismic response control", *J. Struct. Eng.*, **26,** 1427-1433.

Zhang, X.Z., Cheng, F.Y., Jiang, H.P. (2006), "Hybrid actuator–damper–bracing control (HDABC) system with intelligent strategy and soil–structure interaction", *Eng. Struct.*, **28**(4), 2010–2022.

Zhou, N. and Liu, K. (2010), "A tunable high-static-low-dynamic stiffness vibration isolator", *J. Sound Vib.*, **329**(9), 1254-1273.

BS